2024 IEEE International Conference on Robotics and Automation (ICRA 2024)
May 13-17, 2024. Yokohama, Japan

Elliptical torus-based Six-axis FBG Force Sensor with In-situ Calibration for Condition Monitoring of Orthopedic Surgical Robot *

Tianliang Li, *IEEE Senior Member*, Chen Zhao, Yuhang Wen, Fayin Chen, Yuegang Tan, and Zude Zhou

***Abstract*—Six-axis force/moment (6-A F/M) sensors make surgical robots effectively sense intraoperative force feedback and drilling status information, reducing the operating challenges and psychological burden of doctors, which also improves the quality and safety of surgery. However, it is difficult for current commercial electrical 6-A F/M sensors to adapt the electromagnetic environment in the operating room, and status changes after installation can also reduce accuracy. At the same time, there is a strong vibration coupling of low-frequency force information, leading to low identification accuracy and slow response speed in the drilling and milling status. Aiming at these problems, an elliptical torus-based 6-A fiber optic F/M sensor and its in-situ calibration method for orthopedic surgical robot force sensing are proposed. Furthermore, combined with the multichannel one-dimensional convolutional gated recurrent unit (M1-DCGRU), a fast and accurate identification of seven drilling stages was realized. The final force sensing error is less than 7.1%, and the drilling state identification accuracy is at least 93.9%. The designed sensor has higher accuracy, is compatible with magnetic resonance imaging (MRI), and accurately identifies finer drilling stages without relying on other sensors.**

I. INTRODUCTION

Bone drilling surgery plays a vital role in modern medicine and has been used in different surgical fields [1,2]. Traditional surgery relies solely on the surgeon's experience and suffers from low accuracy and safety [3]. Robots have been gradually applied with the increasing maturity of robotic technology to assist orthopedic surgery, which significantly improves surgery safety, efficiency, and accuracy. However, bone is a semi-brittle material, and excessive cutting force is very likely to rupture the bone and transmit it to the inner layer of the bone, which could also cause damage to the soft matrix under the bone [4]. At the same time, the unknown nature of the drilling and milling status poses significant safety issues to the patient [5]. For laminectomy, the tool is required to approach the area within 1 mm of the spinal nerve. Therefore, accurate cutting force sensing and drilling stage identification is crucial to reduce risk and achieve better surgical outcomes [6].

To obtain the force exerted on the bone by the drilling process in open surgery, Kebede *et al*. [7] used a bi-parallel strain gauge to propose a 6-A F/M sensor with excellent dynamic performance and a crosstalk error of 4.78%. Payo *et al*. [8] used 12 strain gauges to involve a 6-A cylindrical F/M sensor and improve the accuracy further and got an average relative error of less than 3%. Although strain gauges are widely used as sensitive units in 6-A F/M sensors because of their high technological maturity [9], the accuracy of strain gauge pasting is strictly required [10]. Capacitive 6-A F/M sensors measure force by changing the gap or area between electrodes [11], effectively avoiding the above problems. He and Liu [12] designed a 6-A F/M sensor using a unique three-dimensional capacitive structure with a maximum error of 0.75%. However, capacitive sensors are very susceptible to electromagnetic interference and incompatible with MRI [13].

Fiber Bragg grating (FBG) force sensors have been widely used in medical robotics due to resistance to electromagnetic interference (EMI) and MRI compatibility [14,15]. Muller *et al*. [16] proposed a Stewart-platformed 6-A FBG F/M sensors for haptic feedback in minimally invasive surgical robots with a conditional number of the sensor's compliance matrix as high as 28.9. Kim *et al*. [17] also proposed a similar sensor structure but with nonlinearities and severe cross-coupling. Li *et al.*[18] have avoided the risk of non-uniform strains in the fiber gate by means of fiber optic suspension, and the sensors that received the influence of the elastomers also showed strong non-linearities and inter-dimensional coupling. To solve the nonlinear problem, Xiong *et al*. [19] achieved low coupling of inter-dimensional forces by designing a four-layer elastomer structure with mechanical decoupling, which not only makes inter-dimensional error less than 2.3% but also increases structural complexity.

In addition, Xiong *et al.* [19] used the weight loading method to realize the calibration of the sensor with complex elastomers, which requires linear and rotary stages to give accurate force and motors to operate the stages. However, the calibration method is not possible to apply accurate moment and continuous force/moment. Li *et al.* [20] propose an eccentric loading calibration method to reduce the complexity of sensor calibration and enable continuous loading. However, the vibration environment in the bone drilling and milling process will cause changes in the sensor state, resulting in significant errors in measurement after long-term sensor operation, and it is still necessary to carry out the calibration method without disassembly to explore. Meanwhile, the sensor structure needs to be more compact and simple while reducing the interdimensional coupling to realize the integrated installation with the robot.

At the same time, the 6-A F/M sensor is also an effective means to obtain the tactile sense of the surgical robot and thus identify the drilling stages. Hu *et al*. [21] developed a surgical robot equipped with a 6-A F/M sensor to identify the five

* This study was supported by the Key R&D Program of Hubei Province under Grant 2022BAA066, and in part by the National Natural Science Foundation of China under Grant 52275541.

Corresponding author: Chen Zhao (zhaochenwhut@whut.edu.cn)

C. Zhao, T. Li, Y. Wen, and F. Chen, are with the School of Mechanical and Electronic Engineering, Wuhan University of Technology, Wuhan, China.

critical stages of laminectomy, which improves the quality of spinal surgery. The mechanical vibration of the bone drilling and milling process often has strong vibrational coupling to low-frequency tactile signals, which causes a significant impact on the identification accuracy of the drill stages [22, 23]. However, the frequency characteristic components of vibration signals vary in different drilling stages, and the combination of vibration signal characteristics can also better realize the identification of drilling stages. Wang *et al*. [24] collected bone drilling vibration signals by installing vibration sensors on the milling cutter and realized the identification of cancellous and cortical bone through the BP neural network. However, the installation of vibration sensors further increases the complexity of the drilling and milling system. Dai *et al*. used a laser displacement sensor to measure the amplitude of the cut bone tissue and extracted the high-frequency component of the vibration signal to realize the identification of bone drilling stages [25]. However, the vibration information extracted from non-contact measurements of displacement signals also suffers from significant errors. In addition, the above method divides into four stages [26] (the drilling and milling stages into the cortical layer, the cancellous layer, the identification of the idling and drilling through stages), which still lacks the identification of the transition stage of each layer, especially the delay of the identification of the drilling out moment will still cause greater damage to human tissues.

Based on the above discussion, this paper proposed an elliptical torus-based 6-A FBG F/M sensor to solve the 6-A F/M sensing problem of bone drilling and milling surgical robots in an MRI interference environment. Considering the state change of the 6-A FBG F/M sensor after mounting to the end of a surgical robot, an in-situ calibration method is proposed. Furthermore, the vibration coupling feature mining in the FBG central wavelength shift signal is realized through the convolutional gated recurrent unit model, and the accurate identification of seven stages of bone drilling and milling surgical robots' bone drilling is realized by relying on the 6-A FBG F/M sensor only. Therefore, the main contributions and advantages of this paper are as follows:

(1) The proposed 6-A FBG F/M sensor can acquire the 6-A F/M of the end-effector of a surgical robot online under the MRI electromagnetic interference environment. The corresponding in-situ calibration method can ensure the in-situ measurement accuracy of this 6-A FBG F/M sensor. Therefore, it can be applied to various surgical robots' end-force sensing.

(2) A bone drilling and milling stage identification method is proposed based on a convolutional gated recurrent unit. The method used the central wavelength shift information under the mechanical vibration of bone drilling and milling to identify different stages of bone drilling and milling without the need for additional acoustic signal sensors and vibration sensors.

II. Sensor Design and Methods

According to the idea of physician tactile bionic design, a 6-A FBG F/M sensor was designed and integrated as a tactile receptor on the robot arm. Furthermore, an M1-DCGRU model was constructed to realize the identification of the drilling stage. The proposed 6-A FBG F/M sensor and bone drilling and milling condition monitoring process are shown in Fig.1.

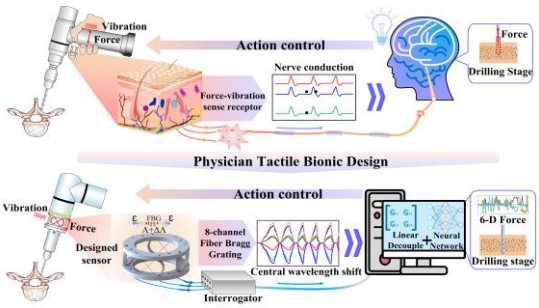

Fig.1 Bone drilling force perception and stage identification

A. Sensor design

The 6-A FBG F/M sensor comprises a double-layer elastomer structure and four cross-suspended optical fibers. Two opposite C-beams are arranged at 90° intervals in the middle of the two layers to form a runway shape, as shown in Fig.2. The distance from the elastomer center to the circle center is 30 mm to make sure that the C-beams fall near the centerline of the loading rings. The inner diameter, outer diameter, and thickness of the connection ring are 50mm, 70mm, and 5mm, respectively. The inner and outer diameter of the C-beam are 8.5mm and 10mm, respectively. In order to ensure the sensitivity and symmetry of the force/mount, the optical fibers are crossed at 90° and arranged inside the two C-beams, and the optical fibers are crossed at 90° and arranged inside the two C-beams. Furthermore, the ends of the optical fibers are offset by 1 mm in the same direction to ensure that the crossed optical fibers do not interfere with the

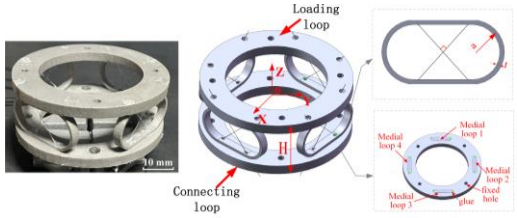

Fig.2 The structure of the designed sensor

sensor when subjected to deformation.

B. Fiber optic sensing principle and in-situ calibration method

The central wavelength shift of the FBG is linearly proportional to the strain. Therefore, the FBG can be used as a sensing element to sense the strain induced by an external force. The 6-A F/M could make the sensor structure deform elastically, resulting in a strain on the FBG.

The associated force and moment components can be derived and calculated from the central wavelength shift of the FBG. The relationship between the central wavelength offset and the strain is as follows for the strain:

$$\Delta\lambda = \lambda_0(1-P_e)\varepsilon \tag{1}$$

where $\Delta\lambda$ and λ_0 are the central wavelength shift of FBG and its initial value, respectively, P_e is the elastic-optic coefficient, ε is the strain of FBG.

The one-dimensional external load is applied to the sensor, and the relationship between the load and the central wavelengths of the eight FBGs can be described as follows:

$$\Delta\lambda_{ij} = \lambda_0(1-P_e)\varepsilon_{ij} = \lambda_0(1-P_e)G_{ij}F_j \tag{2}$$

where $\Delta\lambda ij$ is the central wavelength shift of FBG i, εij is the strain of FBG i when the load F_j is applied to the sensor, G_{ij} is strain response factor.

When the 6-A F/M is applied to the designed sensor, the correlation between the load and the central wavelength shift of the FBG can be expressed as follows:

$$\Delta\lambda = \begin{bmatrix}\Delta\lambda_1\\ \Delta\lambda_2\\ \vdots\\ \Delta\lambda_6\end{bmatrix} = \lambda_0(1-P_e)\begin{bmatrix}G_{11} & G_{12} & \cdots & G_{16}\\ G_{21} & G_{22} & \cdots & G_{26}\\ \vdots & \vdots & \ddots & \vdots\\ G_{61} & G_{62} & \cdots & G_{66}\end{bmatrix}\begin{bmatrix}F_x\\ F_y\\ \vdots\\ M_z\end{bmatrix} = KF \tag{3}$$

where $\Delta\lambda$ is the wavelength variation vector, and K is the sensitivity characteristic matrix.

6-A FBG F/M sensors are subject to large deviations after mounting on the end of a surgical robot due to the mounting state and other influences. Therefore, a two-stage calibration method is used to achieve in-situ calibration of the sensors without disassembly. Based on the existing calibration matrix, the parameters of the existing calibration matrix are corrected to solve the in-situ calibration matrix by a small amount of in-situ measurement data. This method reduces the error caused by the change of sensor installation state and overcomes the requirement on the amount of data.

$$\begin{aligned} F_L^S(x) &= \alpha_1 \cdot F_L(x) + \alpha_2 \cdot F_L^*(x)\\ &= \begin{bmatrix}\alpha_1 C_{11}+\alpha_2 C_{11}^* & \alpha_1 C_{12}+\alpha_2 C_{12}^* & \cdots & \alpha_1 C_{18}+\alpha_2 C_{18}^*\\ \alpha_1 C_{21}+\alpha_2 C_{21}^* & \alpha_1 C_{22}+\alpha_2 C_{22}^* & \cdots & \alpha_1 C_{28}+\alpha_2 C_{28}^*\\ \vdots & \vdots & \ddots & \vdots\\ \alpha_1 C_{61}+\alpha_2 C_{61}^* & \alpha_1 C_{62}+\alpha_2 C_{62}^* & \cdots & \alpha_1 C_{68}+\alpha_2 C_{68}^*\end{bmatrix}\begin{bmatrix}\Delta\lambda_1\\ \Delta\lambda_2\\ \vdots\\ \Delta\lambda_8\end{bmatrix}\\ &= C_{6\times6}C_L\Delta\lambda \end{aligned} \tag{4}$$

The solution of the parameter correction matrix $C_{6\times6}$ can be solved by least squares fitting:

$$\arg\min_C \frac{1}{N}\sum_i^N \left\| F_L^S(x) - C_{6\times6}C_L\Delta\lambda \right\|^2 \tag{5}$$

C. Drilling stage identification method

Since the input to the convolutional layer is a multi-channel signal, a multi-channel convolutional kernel is used for feature extraction. Meanwhile, it is necessary to calculate the weighted sum of the results of each channel at the exact location and get the results of the convolutional computation of the network of the layer. The calculation process is as follows:

$$x^l = \sum_{j-1}^{m} w_j \times f_j\left(\sum_{i-1}^{k}(x_{ij}^{l-1} * w_{ij}^{l-1}) + b_{ij}^{l-1}\right) \tag{6}$$

where x^l is the output of the lth convolutional layer, x_{ij}^{l-1} is the j^{th} character input of the $(l\text{-}1)^{th}$ convolutional layer of channel j, with k character inputs, w_{ij}^{l-1} the i^{th} convolutional kernel of the $(l\text{-}1)^{th}$ layer of channel j, b_{ij}^{l-1} is the ith bias value of the $(l\text{-}1)^{th}$ layer of channel j, f is the nonlinear activation function, and m is the number of channels.

Considering the length of the input time series signal, a gated recurrent unit is further introduced to capture the timing characteristics. The gated recurrent unit is a chain propagation network, and the inputs of the neurons at the t moment are the input layer data and the hidden state output at the t-1 moment. The hidden state of the current moment and the output of the output layer are obtained by neuronal computation, which makes the network regarded as an infinitely repeated neural structure. The mathematical model can be expressed as:

$$\begin{cases} r_t = \sigma(w_{rh}h_{t-1} + w_{rx}x_t)\\ z_t = \sigma(w_{zh}h_{t-1} + w_{zx}x_t)\\ \tilde{h}_t = \tanh(w_{hh}(r * h_{t-1}) + w_{hx}x_t)\\ h_t = (1-z_t) * \tilde{h}_t + z_t * h_{t-1}\end{cases} \tag{7}$$

where r_t is the output of the reset gate at moment t, z_t is the output of the update gate at moment t, w is the unit calculation weights, h_t is the hidden state output at the moment t, and $\tilde{h}_t$ candidate hidden state output at the moment t, tanh and σ are the activation function.

The constructed M1-DCGRU classification model network parameters and models are shown in Tab.1 and Fig.3.

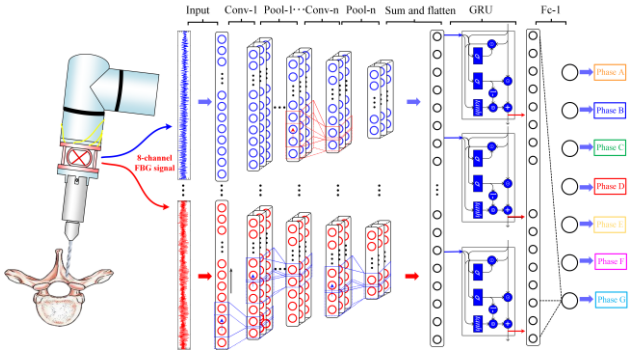

Fig.3 The structure of the M1-DCGRU classification model

Tab.1 M1-DCGRU network parameters

Layer	*Kernel size*	*Input*	*Output*	*Stride*	*Activation*
Conv1d	32*1	7	16	1	Tanh
Pool1d	2*1	16	16	2	-
Conv1d	5*1	16	32	1	Tanh
Pool1d	2*1	32	32	2	-
Conv1d	3*1	32	128	1	ReLU
Conv1d	3*1	128	256	1	ReLU
GRU	-	256	256	-	-

III. Experiments And Results

A. Off-situ calibration

In order to realize the calibration of the sensor, a 6-A FBG F/M sensor calibration experimental setup was built, as shown in Fig.4. The cross-shaped calibration bracket was mounted on the top of the 6-A FBG F/M sensor and connected to the z-axis of the SRI sensor by a nylon rope. The force calibration process was loaded from 0 N to 100 N with a step of 10 N. The calibration process for moments was performed using eccentric loading, for -Fy coupled to ±Mz, Fz coupled to ±Mx, and Fz coupled to ±My. Since the force arm length of the calibration cross is 50mm, the calibration loading is done (100 N·mm) from 0 N to 20 N (1000 N·mm) with a step of 2 N.

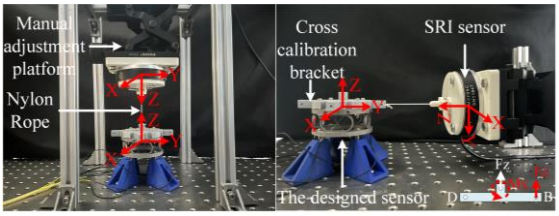

Fig.4 Setup for off-situ calibration

The wavelength shift of the FBG and the reference force of the SRI were obtained by simultaneous acquisition using the self-developed Labview acquisition software. The data from the four tests were averaged and plotted as a curve, as shown in Fig.5.The calibration matrix $C_{6\times8}$ with linear least squares optimum is obtained by calculating the pseudo-inverse of λ, as shown in Tab.2. Substituting the experimental data into the calibration matrix yields class I errors (nonlinear errors) of 0.821%, 1.182%, 0.588%, 2.169%, 2.583%, and 1.044%, respectively. And the class II errors are calculated as 2.537%, 2.483%, 3.178%, 6.616%, 9.461%, and 4.701%, respectively. These performances effectively validate the feasibility of the 6-A FBG F/M sensor.

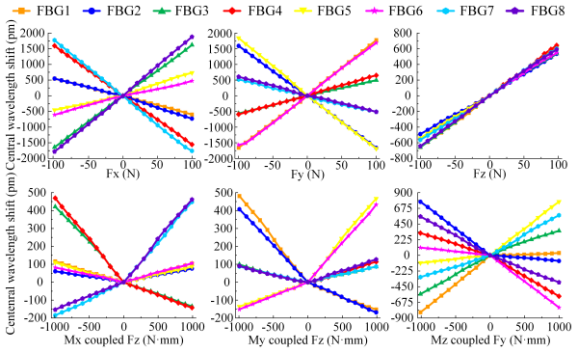

Fig.5 Wavelength shift caused by the applied force.

Tab.2 Calibration matrix (10^{-3})

-1.0	-1.7	15.7	-13.2	-1.6	-1.6	-13.8	15.4
16.7	-19.4	-3.6	2.7	-12.1	10.6	-2.9	2.0
13.7	26.9	28.9	17.2	15.3	25.2	25.1	16.5
231.2	-307.3	-788.5	-817.6	-268.8	259.9	832.3	803.5
-1006.7	-618.2	-60.4	86.0	598.8	1038.5	447.4	-441.6
220.8	-245.2	332.6	-352.0	240.3	-194.4	307.7	-333.4

B. In-situ calibration

In-situ calibration experiments were performed on the sensors using the UR5 robotic arm platform, as shown in Fig.6. The designed sensor was mounted to the UR5 robotic arm, and the SRI sensor was fixed to the optical platform to provide a reference force/moment. Two calibration crosses with a force arm radius of 50 mm were mounted on the two sensors, and the x-positive half-axis of both sensors was connected by a spring to transmit the force. The designed sensor driven by UR5 was operated on a circle with a radius of 140 mm at different latitudes ranging from 25° to 85°N. Only the 25° latitude data were used to correct the previous calibration matrix. The central wavelength shift data of the designed sensor has been collected and converted into F/M information by two calibration matrices.

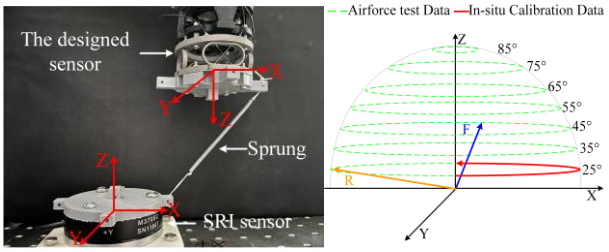

Fig.6 Setup for in-situ calibration

Fig.7 plots the previous calibration matrix decoupled 6-A F/M curves (25°~85°) against the in-situ calibration matrix solved 6-A F/M curves (25°~85°). After the pair of two calibration methods were solved, the measurement results of the designed sensor were basically consistent with the reference results of the SRI sensor. However, the offset of the F/M curve solved by the off-situ calibration matrix is significantly larger than that of the in-situ calibration matrix.

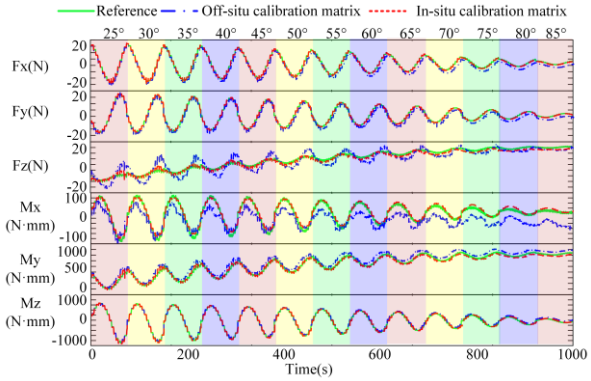

Fig.7 Comparison of referenced F/M, the original output F/M of off-situ calibration, and the output F/M of in-situ calibration

The 6-A F/M error curves are shown in Fig.8, and the previous calibration matrix decoupled 6-A F/M relative errors at full scale for each dimension are 3.30%, 3.87%, 5.72%, 6.25%, 12.50%, and 7.13%, respectively. After in-situ calibration with a small amount of low-latitude data, the full-scale relative errors of each dimension of the multidimensional force were reduced to 1.60%, 0.88%, 1.56%, 1.95%, 7.10%, and 2.54%. These results validate the feasibility and effectiveness of the in-situ calibration method.

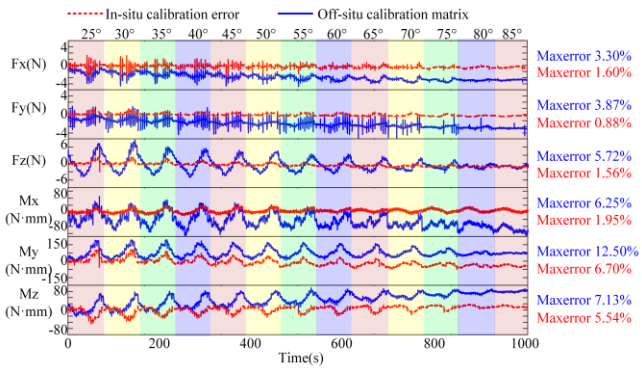

Fig.8 Comparison of 6-A F/M solving errors between off-situ calibration and in-situ calibration

C. *Auxiliary Bone Drilling and Milling Experiment*

The effectiveness of the designed sensor was verified by robot-assisted bone drilling experiments, as shown in Fig.9. The bone was drilled with different angles (30°, 60°, and 30°) to simulate drilling on various surfaces during surgery. The diameter of the twist drill was 2.2 mm, and the feed rate was 0.5 mm/s. In order to construct a subsequent identification model for the bone drilling stage, all 16 cut scapulae were drilled 5-10 times to collect a total of 116 times drilling data. The picture of the bone after drilling is shown as follows:

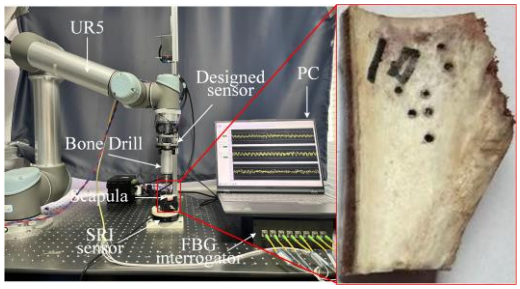

Fig.9 Robot-assisted bone drilling and milling experiment

Considering the vibration coupling interference during bone drilling, the central wavelength shift was processed by the smooth smoothing processing function, and the filtered combined force signal was solved, as shown in Fig.10. It can be seen that the maximum combined force errors in the three drilling experiments are 0.62N, 0.58N, and 1.13N, respectively. The results verified that the designed sensor can be used to measure the orthopedic surgical robot's drilling force.

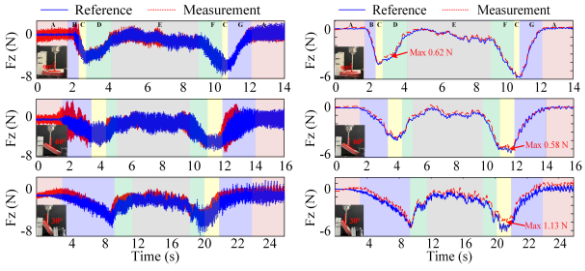

(a) F decoupling vibration (b) F after filtering

Fig.10 Force monitoring during bone drilling

Since the vibration feature components in the frequency domain signals are not the same at different stages, the drilling stage could be inverted by the vibration information of the 6-A F/M change curve species. Therefore, the stage prediction can be regarded as a pattern identification problem, and the raw data of the central wavelength shift of 8 FBGs are used as the data source to identify the drilling status.

The 8-channel central wavelength shift data are divided into samples of length 100~1000, and the ratio between training and testing data is 3:1. The model accuracies trained on samples of different data lengths are compared to determine the optimal sample data volume. The error bar graph curve of the average result of 10 training is shown in Fig.11. It can be seen that the model accuracy varies lowly with the increase in sample length when the sample length reaches 500. At the same time, considering the single-channel sampling frequency of the demodulator is 2000 Hz, the time scale of the drilling stage identification is the number of sample points S/2000 s. The dataset's sample length is set to 500 by taking into account the model's response speed and accuracy. Therefore, the size of each dataset is 500×8, and the time scale for the drilling depth identification is 0.25s.

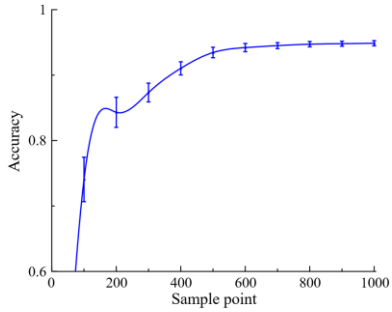

Fig.11 Identification accuracy mapped to sample length

40 samples were randomly selected from various data types to form the training set, and the remaining 120 data were used as the training set. The model achieves convergence after 150 training generations, and accuracy fluctuations occur during the subsequent training process, as shown in Fig.12(a). The optimal model was selected as the drill stages identification model during the training process, and the accuracy of its corresponding test set is 93.9%. Its confusion matrix is shown in Fig.12(b), the identification accuracies of the model at each stage are 100%, 95.0%, 87.5%, 95.0%, 97.5%, 90.0%, and 92.5%, which verified the effectiveness of the drill status identification model.

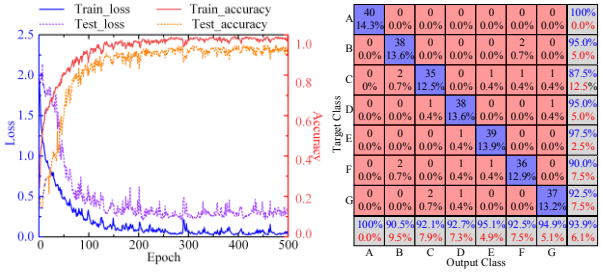

(a) Model Training Curve (b) Confusion matrix of test data

Fig.12 Drilling phase identification accuracy

IV. Discussion and Conclusion

In this work, we have investigated the construction of An elliptical torus based 6-A FBG F/M sensor for bone drilling surgical robot force sensing and feedback. However, the curves of the symmetrical two fibers in Fig.5 cannot completely overlap during loading because of the assembly and manufacturing errors. At the same time, the sensitivity of the fiber in the z-dimensional is also different. Improved assembly and manufacturing accuracy can help further address this issue and improve sensitivity.

In addition, the metal 3D printing preparation process reduces the cost and manufacturing difficulty of the sensor. The sensor is also suitable for MRI-guided bone drilling and milling surgery. Therefore, sensor has the advantage of low-cost, resistant to electromagnetic interference, and effectively compatible with MRI. The proposed in-situ calibration method effectively solves the problem of the sensor's accuracy degradation after a long period and is more straightforward and effective than the traditional calibration method. A robot-assisted bone drilling experiment is carried out based on the sensor, which realizes the force sensing in the drilling process. Combined with the proposed M1-DCGRU model, the fast and accurate identification of seven drilling stages is realized without the help of other sensors.

Considering the constant temperature environment in the operating room, the sensor is not temperature compensated in this work. Therefore, the goal of future work is to realize the control of drilling and milling operations in combination with this sensor and to realize the temperature compensation of this sensor. At the same time, the bone drilling stage identification model needs to be tested for online monitoring applications.

References

[1] Y. Torun, O. Pazarci, and A. Ozturk, "Current Approaches to Bone-Drilling Procedures with Orthopedic Drills," *Cyprus Journal of Medical Sciences*, 2020, vol.5, no.1, pp.93–98.

[2] Y. Torun, and A. Ozturk, "A New Breakthrough Detection Method for Bone Drilling in Robotic Orthopedic Surgery with Closed-Loop Control Approach," *Annals of Biomedical Engineering*, 2020, vol.48, pp.1218–1229.

[3] C. Xu, L. Lin, Z. M. Aung, G. Chai, and L. Xie, "Research on spatial motion safety constraints and cooperative control of robot-assisted craniotomy: Beagle model experiment verification," *The International Journal of Medical Robotics and Computer Assisted Surgery*, 2021, vol.17, no.2, pp.2231.

[4] A. Niesche, M. Muller, F. Ehreiser, D. Teichmann, S. Leonhardt, and K. Radermacher, "Smart bioimpedance-controlled craniotomy: Concept and first experiments, Proceedings of the Institution of Mechanical Engineers," *Part H: Journal of Engineering in Medicine*, 2017, vol.231, no.7, pp.673-680.

[5] Y. Dai, Y. Xue, and Jianxun Zhang, "Vibration-based milling condition monitoring in robot-assisted spine surgery," *IEEE/ASME Transactions on Mechatronics*, 2015, vol.20, no.6, pp.3028-3039.

[6] J. J. Doulgeris, S. A. Gonzalez-Blohm, A. K. Filis, T. M. Shea, K. Aghayev, and F. D. Vrionis, "Robotics in neurosurgery: evolution, current challenges, and compromises," *Cancer Control*, 2015, vol.22, no.3, pp.352-359.

[7] G. A. Kebede, A. R. Ahmad, S. C. Lee, and C. Y. Lin, "Decoupled six-axis force–moment sensor with a novel strain gauge arrangement and error reduction techniques," *Sensor*, 2019, vol.19, no.13, pp.19133012.

[8] I. Payo, J. M. Adánez, D. R. Rosa, R. Fernández, and A. S. Vázquez, "Six-axis column-type force and moment sensor for robotic applications," *IEEE Sensors Journal*, 2018, vol.18, no.17, pp.6996-7004.

[9] C. Y. Lin, A. R. Ahmad, and G. A. Kebede, "Novel mechanically fully decoupled six-axis force-moment sensor," *Sensors*, 2020, vol.20, no.2, pp.20020395.

[10] U. Kim, Y. B. Kim, J. So, and H. R. Choi, "Novel mechanically fully decoupled six-axis force-moment sensor," *International Conference on Ubiquitous Robots and Ambient Intelligence (URAI)*, 2017, pp.268-270.

[11] A. Song, and L. Y. Fu, "Multi-dimensional force sensor for haptic interaction: A review," *Virtual Reality & Intelligent Hardware*, 2019, vol.1, no.2, pp.121-135.

[12] H. Zexia and T. Liu, "Design of a three-dimensional capacitor-based six-axis force sensor for human-robot interaction," *Sensors and Actuators A: Physical*, 2021, vol.331, pp.112939.

[13] M. Y. Cao, S. Laws, and F. R. Baena, "Six-axis force/torque sensors for robotics applications: A review," *IEEE Sensors Journal*, 2021, vol.21, no.24, pp.27238-27251.

[14] W. J. Lai, L. Cao, R. X. Tan, P. T. Phan, J. Z. Hao, S. C. Tjin, and S. J. Phee, "Force sensing with 1 mm fiber Bragg gratings for flexible endoscopic surgical robots," *IEEE/ASME Transactions on Mechatronics*, 2019, vol.25, no.1, pp.371-382.

[15] T. L. Li, N. K. King, and H. L. Ren, "Disposable FBG-based tridirectional force/torque sensor for aspiration instruments in neurosurgery," *IEEE Transactions on Industrial Electronics*, 2019, vol.67, no.4, pp.3236-3247.

[16] M. S. Müller, L. Hoffmann, T. C. Buck, and A. W. Koch, "Fiber Bragg grating-based force-torque sensor with six degrees of freedom," *International Journal of Opto-mechatronics*, 2009, vol.3, no.3, pp.201-214.

[17] C. Kim, and C. H. Lee, "Development of a 6-AoF FBG force–moment sensor for a haptic interface with minimally invasive robotic surgery," *Journal of Mechanical Science and Technology*, 2016, vol.30, pp. 3705-3712.

[18] T. L. Li, J. X. Guo, H. Zheng, S. S. Wang, L. Qiu, and H. L. Ren, "Fault-Tolerant Six-Axis FBG Force/Moment Sensing for Robotic Interventions," *IEEE/ASME Transactions on Mechatronics*, 2023. (Early Access)

[19] L. Xiong, Y. X. Guo, G. Z. Jiang, X. L. Zhou, L. Jiang, and H. H. Liu, "Six-dimensional force/torque sensor based on fiber Bragg gratings with low coupling," *IEEE Transactions on Industrial Electronics*, 2020, vol.68, no.5, pp.4079-4089.

[20] T. L. Li, F. Y. Chen, Z. B. Zhao, Q. F. Pei, Y. G. Tan, and Z. D. Zhou, "Hybrid Data-Driven Optimization Design of a Layered Six-Dimensional FBG Force/Moment Sensor With Gravity Self-Compensation for Orthopedic Surgery Robot," *IEEE Transactions on Industrial Electronics*, 2023, vol.70, no.8, pp.8568-8579.

[21] L. Li, B. C. Yu, C. Yang, P. Vagdargi, R. A. Srivatsan, and H. Choset, "Development of an inexpensive tri-axial force sensor for minimally invasive surgery," *IEEE/RSJ International Conference on Intelligent Robots and Systems (IROS)*, 2017, pp.906-913.

[22] Y. Dai, Y. Xue, and J. X. Zhang, "Milling state identification based on vibration sense of a robotic surgical system," *IEEE Transactions on Industrial Electronics*, 2016, vol.63, no.10, pp.6184-6193.

[23] Y. Dai, Y. Xue, and J. X. Zhang, "Vibration Feedback Control for Robotic Bone Milling," *IEEE Transactions on Industrial Electronics*, 2022, vol.70, no.10, pp.10312-10322.

[24] J. G. Wang, G. M. Xia, Y. Dai and J. X. Zhang, "Bone cutting status detection based on vibration sensor array," *Chinese Control Conference* (*CCC*), 2021, pp.4193-4197.

[25] Y. Dai, Y. Xue, and J. X. Zhang, "Vibration-based milling condition monitoring in robot-assisted spine surgery," *IEEE/ASME Transactions on Mechatronics*, 2015, vol.20, no.6, pp. 3028-3039.

[26] Y. Dai, Y. Xue, and J. X. Zhang, "Bioinspired integration of auditory and haptic perception in bone milling surgery," *IEEE/ASME Transactions on Mechatronics*, 2018, vol.23, no.2, pp.614-623.